A Born–WKBJ Pre-Stack Seismic Inversion Based on a 3-D Structural-Geology Model Building

Cong Luo, Jing Ba, Guangtan Huang, and José M. Carcione

***Abstract*— Estimation of subsurface properties by using the scattering integral equation is a method that finds increasing use in near-surface and shallow oil/gas exploration, based on seismic, low-frequency electromagnetic, and surface-radar surveys. The method can accurately simulate physical realizations induced by small-scale perturbations, but its accuracy depends on a suitable low-frequency property model. We propose a 3-D geological-structure-guided model building to provide a reliable low-frequency model and combine it with the Born–Wentzel–Kramers–Brillouin–Jeffreys (WKBJ)-approximation-based inversion algorithm. Instead of the traditional approach based on artificially interpreted horizons, we use 3-D seismic-slope attributes as lateral constraints, which contain more geological information. Plane-wave destruction (PWD) in 3-D is exploited to extract the 2-D slopes along the inline and crossline directions, which are the key factors in computing 3-D slopes. Then, by introducing the shaping regularization, we build low-frequency models by solving the inverse problem. Numerical analysis indicates that an appropriate background model is essential for seismic modeling with the Born–WKBJ approximation. The methodology is applied to synthetic and 3-D field data, and the examples show that it provides reliable background models and improves the inversion performance.**

***Index Terms*— 3-D structure constraints, Born–Wentzel–Kramers–Brillouin–Jeffreys (WKBJ) approximation, model building, pre-stack seismic inversion.**

I. Introduction

PRE-STACK seismic inversion with amplitude-versus-offset (AVO) or amplitude-versus-angle (AVA) techniques is widely adopted to extract subsurface properties from seismic data. The AVO/AVA modeling and corresponding inversion can be classified into two main categories, namely ray-tracing and wave-equation methods [1]. The first is based on a single-interface assumption and the most common are the Zoeppritz equation and its approximations for isotropic media, and the Rüger simplified equation in the anisotropic case [1]. Wave-equation methods based on an analytical or approximate solution to the wave equation obtain the full wavefield [1]–[6]. Compared with ray-tracing methods [7]–[12], the second approach considers the amplitudes and phases of primary reflections, converted waves, multiples and converted modes [13]–[15].

Although wave-equation-based pre-stack inversion is not new [16], [17], it is finding increasing application in geophysics with the latest developments in computer technology. The inversion consists in minimizing the misfit between the measured and synthetic data under certain constraints [12], [18], where the forward operator plays an essential role [3]. The wave-equation-based modeling can be numerical [19] or analytical [1], [13], [14], [20]. Generally, the second, including the reflectivity method, Green's function (in the homogeneous cases), or propagator matrix, uses a 1-D model and an analytical solution [21]–[23]. However, in the case of complex structures and lithologies, numerical modeling, such as finite differences and finite elements, is better suited for the inversion. Its inversion, namely full waveform inversion (FWI) [19], has been developed for decades, but limited by the high computational complexity. Thus, the target-oriented waveform inversion is mainly based on the analytical modeling and called pre-stack waveform inversion (PWI) [1], [4], [6], [14].

Due to the strong nonlinear relationship between the synthetic data and properties (parameters), the PWI usually is based on a nonlinear optimization, such as simulated annealing [5] and genetic algorithm [14]. In order to improve the computational efficiency, the Fréchet derivative (the partial derivative of the forward operator with respect to the model parameters) is employed, which is required to use gradient-based linear optimization [1], [3], [4], [6], [15]. However, calculating the Fréchet gradient of a nonlinear forward operator is time-consuming and mathematically complex. Therefore, the researchers linearize the wave-equation modeling.

The wavefield can be computed with the Lippmann–Schwinger equation based on the Wentzel–Kramers–Brillouin–Jeffreys (WKBJ) approximation, even for strongly inhomogeneous media [24]–[26]. Analytical solutions based on the Green function are difficult to obtain in this case [27], [28]. The WKBJ is a high-frequency approximation and neglects the coupling between wave modes. Therefore, the solution of the Lippmann–Schwinger equation is an

Manuscript received January 15, 2021; revised July 2, 2021; accepted August 2, 2021. This work was supported in part by the National Natural Science Foundation of China under Grant 42004111; in part by China Postdoctoral Science Foundation under Grant 2021T140175, Grant 2019M661716, and Grant 2020M681860; in part by the Fundamental Research Funds for the Central Universities of China under Grant B200202135; in part by Jiangsu Innovation and Entrepreneurship Plan; and in part by Jiangsu Province Science Fund for Distinguished Young Scholars. *(Corresponding author: Jing Ba.)*

Cong Luo and Jing Ba are with the Department of Geological Engineering, Hohai University, Nanjing 211100, China (e-mail: jba@hhu.edu.cn).

Guangtan Huang is with the State Key Laboratory of Geomechanics and Geotechnical Engineering, Institute of Rock and Soil Mechanics, Chinese Academy of Sciences, Wuhan 430071, China.

José M. Carcione is with the National Institute of Oceanography and Applied Geophysics (OGS), 34010 Trieste, Italy, and also with the Department of Geological Engineering, Hohai University, Nanjing 211100, China.

Digital Object Identifier 10.1109/TGRS.2021.3103430

approximation, but its solution requires to invert a matrix, leading to a high computation cost, especially for high-dimensional models [29]–[31]. Thus, the Born approximation is used, based on a Taylor expansion and retaining the first-order term, which accelerates the algorithm [32]–[35]. The accuracy of the Born–WKBJ approximation highly depends on the intermediate wavefield generated with the low-frequency background medium [36]–[38].

In the FWI, there are several approaches to obtain a low-frequency velocity model. For uniform-density acoustic inversion, the low-frequency model is based on the P-wave velocity, which is obtained with classical velocity analysis [39]. Tomography is another, more accurate choice, solving an inverse problem to update the velocity model [40]–[42]. However, the accuracy of these approaches depends, to a great extent, on the quality of the seismic data. Chen *et al.* [43] proposed a new model building method for FWI, performing a well-log interpolation constrained by the 2-D geological structure attribute (local plane-wave slope).

For the pre-stack inversion, low-frequency initial models are built by routinely interpolating well data along manually interpreted horizons, which provides the spatial morphology of the subsurface structure to some extent. This approach considers a limited number of geological elements and may fail in the case of existing unusual geological bodies, such as salt domes and volcanic intrusions. Besides, it requires a large amount of workloads and introduces artificial errors, especially for complex geological conditions [18], [44]. To overcome these problems, Huang *et al.* [44] introduced a 2-D seismic-slope-regularized model building method into pre-stack seismic inversion and achieved good results. However, this method is only applicable to 2-D data and a 3-D approach is required, since not all the seismic lines cross the wells, and the slope of a spatial sample may not be along the direction of a single line.

We propose a 3-D data-driven model building method regularized by 3-D seismic slope attributes, obtained with a plane-wave destruction (PWD) [45], [46], and exploit the reshaping regularization to achieve a reliable model. Then, we introduce this algorithm into the Born–WKBJ-approximation-based PWI, a method highly affected by the given low-frequency model, to improve the inverted results.

This article is organized as follows. First, we briefly review the modeling and inversion theories based on the scattering integral and introduce the 3-D geological-structure-guided well-log interpolation. Second, we investigate the effect of the background and initial models on the modeling and inversion results, using the synthetic examples. Then, the 3-D Claerbout's "qdome" model is exploited to test the proposed model building method. Finally, we combine the model building with the Born–WKBJ approximation and apply the methodology to field data.

II. Theory and Methodology

A. Born-Approximation Modeling

According to the elastic wave propagation theory, wave motion can be expressed by the first-order velocity–stress wave equation

$$-\Delta_{kmpq}\partial_m\tau_{pq} + \partial_t\rho\upsilon_k = f_k \tag{1a}$$
$$\Delta_{ijmr}\partial_m\upsilon_r - \partial_t S_{ijpq}\tau_{pq} = h_{ij} \tag{1b}$$

where τ and υ represent stress/force and particle velocity, S_{ijpq} are the components of the compliance tensor, ρ denotes the bulk density, f and h represent external force and stress-rate source, respectively, and ∂ denotes the partial differential operator. We transform (1) *into* the frequency-wavenumber domain to obtain

$$-ik_m\Delta_{kmpq}\tau_{pq} + i\omega\rho\upsilon_k = f_k \tag{2a}$$
$$ik_m\Delta_{ijmr}\upsilon_r - i\omega S_{ijpq}\tau_{pq} = h_{ij} \tag{2b}$$

where ω and k denote the angular frequency and wavenumber, respectively.

According to de Hoop *et al.* [47], the symmetrical tensors of rank 2 in (2) can be decomposed into their omnidirectional and deviatoric parts as follows:

$$i\omega\rho\upsilon_k - ik_m\left(\tau^{\sigma}_{km} + \tau^{+\backslash\sigma}_{km}\right) = f_k \tag{3a}$$
$$ik_n\Delta^{\sigma}_{ijnr}\upsilon_r - i\omega S^{\sigma,\sigma}_{ijpq}\tau^{\sigma}_{pq} = h^{\sigma}_{ij} \tag{3b}$$
$$ik_n\Delta^{+\backslash\sigma}_{ijnr}\upsilon_r - i\omega S^{+\backslash\sigma,+\backslash\sigma}_{ijpq}\tau^{+\backslash\sigma}_{pq} = h^{+\backslash\sigma}_{ij}. \tag{3c}$$

By introducing the background properties S_0 and ρ_0, we rewrite (3) as

$$\begin{aligned} &i\omega\upsilon_k - ik_m\frac{1}{\rho_0}\left(\tau^{\sigma}_{km} + \tau^{+\backslash\sigma}_{km}\right)\\ &\quad = ik_m\left(\frac{1}{\rho} - \frac{1}{\rho_0}\right)\left(\tau^{\sigma}_{km} + \tau^{+\backslash\sigma}_{km}\right) \end{aligned} \tag{4a}$$
$$\begin{aligned} &-i\omega\tau^{\sigma}_{pq} - ik_n\frac{1}{S^{\sigma,\sigma}_{0,ijpq}}\Delta^{\sigma}_{ijnr}\\ &\quad = ik_n\left(\frac{1}{S^{\sigma,\sigma}_{ijpq}} - \frac{1}{S^{\sigma,\sigma}_{0,ijpq}}\right)\Delta_{ijnr}\upsilon_r \end{aligned} \tag{4b}$$
$$\begin{aligned} &-i\omega\tau^{+\backslash\sigma}_{pq} - ik_n\frac{1}{S^{+\backslash\sigma,+\backslash\sigma}_{0,jipq}}\Delta^{\sigma}_{ijnr}\upsilon_r\\ &\quad = ik_n\left(\frac{1}{S^{+\backslash\sigma,+\backslash\sigma}_{ijpq}} - \frac{1}{S^{+\backslash\sigma,+\backslash\sigma}_{0,ijpq}}\right)\Delta_{ijnr}\upsilon_r. \end{aligned} \tag{4c}$$

Moreover, for isotropic elastic media, the compliance tensor S can be written as

$$S^{\sigma,\sigma}_{ijpq} = \Lambda\Delta^{\sigma}_{ijpq}, \quad S^{+\backslash\sigma,+\backslash\sigma}_{ijpq} = M\Delta^{\sigma}_{ijpq} \tag{5}$$

where

$$\Lambda = \frac{1}{3\lambda + 2\mu}, \quad M = \frac{1}{2\mu}. \tag{6}$$

According to the Lippmann–Schwinger integral equation, the total field in the perturbed medium $\mathbf{P} = \left[-\boldsymbol{\tau}^{\sigma}, -\boldsymbol{\tau}^{+\backslash\sigma}, \mathbf{v}\right]^{\mathrm{T}}$ can be set as the sum of two parts, that is, the background wavefield $\mathbf{P}_0$ and the scattering wavefield $\mathbf{P}_{\mathrm{S}}$

$$\mathbf{P}\left(k_x, k_y, k_z, \omega\right) = \mathbf{P}_0\left(k_x, k_y, k_z, \omega\right) + \mathbf{P}_{\mathrm{S}}\left(k_x, k_y, k_z, \omega\right). \tag{7}$$

On the other hand, the field generated by a point source can be represented by Green functions, $\mathbf{G}$, as

$$\begin{aligned}-\boldsymbol{\tau}^{\sigma}_{0,pq}(\mathbf{r}) &= \int \Big[\mathbf{G}^{\sigma,\sigma}_{0,pqij}(\mathbf{r}-\mathbf{r}_{\mathrm{S}})\cdot\mathbf{h}^{\sigma}_{ij} + \mathbf{G}^{\sigma,+\backslash\sigma}_{0,pqij}(\mathbf{r}-\mathbf{r}_{\mathrm{S}})\cdot\mathbf{h}^{+\backslash\sigma}_{ij} \\ &\qquad + \mathbf{G}^{\sigma,f}_{0,pqk}(\mathbf{r}-\mathbf{r}_{\mathrm{S}})\cdot\mathbf{f}_k\Big]d\mathbf{r} \qquad (8a)\end{aligned}$$

$$\begin{aligned}-\boldsymbol{\tau}^{+\backslash\sigma}_{0,pq}(\mathbf{r}) &= \int \Big[\mathbf{G}^{+\backslash\sigma,\sigma}_{0,pqij}(\mathbf{r}-\mathbf{r}_{\mathrm{S}})\cdot\mathbf{h}^{\sigma}_{ij} + \mathbf{G}^{+\backslash\sigma,+\backslash\sigma}_{0,pqij}(\mathbf{r}-\mathbf{r}_{\mathrm{S}})\cdot\mathbf{h}^{+\backslash\sigma}_{ij} \\ &\qquad + \mathbf{G}^{+\backslash\sigma,f}_{0,pqk}(\mathbf{r}-\mathbf{r}_{\mathrm{S}})\cdot\mathbf{f}_k\Big]d\mathbf{r} \qquad (8b)\end{aligned}$$

$$\begin{aligned}\mathbf{v}_{0,r}(\mathbf{r}) &= \int \Big[\mathbf{G}^{v,\sigma}_{0,rij}(\mathbf{r}-\mathbf{r}_{\mathrm{S}})\cdot\mathbf{h}^{\sigma}_{ij} + \mathbf{G}^{v,\sigma}_{0,rij}(\mathbf{r}-\mathbf{r}_{\mathrm{S}})\cdot\mathbf{h}^{+\backslash\sigma}_{ij} \\ &\qquad + \mathbf{G}^{v,f}_{0,rk}(\mathbf{r}-\mathbf{r}_{\mathrm{S}})\cdot\mathbf{f}_k\Big]d\mathbf{r} \qquad (8c)\end{aligned}$$

or, in matrix form

$$\begin{bmatrix}-\boldsymbol{\tau}^{\sigma}_{0,pq}\\ -\boldsymbol{\tau}^{+\backslash\sigma}_{0,pq}\\ \mathbf{v}_{0,r}\end{bmatrix} = \int \begin{bmatrix}\mathbf{G}^{\sigma,\sigma}_{0,pqij} & \mathbf{G}^{\sigma,+\backslash\sigma}_{0,pqij} & \mathbf{G}^{\sigma,f}_{0,pqk}\\ \mathbf{G}^{+\backslash\sigma,\sigma}_{0,pqij} & \mathbf{G}^{+\backslash\sigma,+\backslash\sigma}_{0,pqij} & \mathbf{G}^{+\backslash\sigma,f}_{0,pqk}\\ \mathbf{G}^{v,\sigma}_{0,rij} & \mathbf{G}^{v,+\backslash\sigma}_{0,rij} & \mathbf{G}^{v,f}_{0,rk}\end{bmatrix}(\mathbf{r}-\mathbf{r}_{\mathrm{S}})\begin{bmatrix}\mathbf{h}^{\sigma}_{ij}\\ \mathbf{h}^{+\backslash\sigma}_{ij}\\ \mathbf{f}_k\end{bmatrix}d\mathbf{r} \qquad (9)$$

where $\mathbf{r}_{\mathrm{S}}$ is the location of the source. $\mathbf{G}^{\sigma,\sigma}_{pqij}$, $\mathbf{G}^{+\backslash\sigma,\sigma}_{pqij}$, $\mathbf{G}^{\sigma,+\backslash\sigma}_{pqij}$, and $\mathbf{G}^{+\backslash\sigma,+\backslash\sigma}_{pqij}$ are the stress/deformation rate source Green functions, $\mathbf{G}^{\sigma,f}_{pqk}$ and $\mathbf{G}^{+\backslash\sigma,f}_{pqk}$ are the stress/force source ones, $\mathbf{G}^{v,\sigma}_{rij}$ and $\mathbf{G}^{v,+\backslash\sigma}_{rij}$ are the particle velocity/deformation rate source ones, and $\mathbf{G}^{v,f}_{rk}$ is the particle-velocity/force one [37], [38]. The expressions in components are

$$\begin{aligned}G^{\sigma,\sigma}_{pqij}(\mathbf{r}) &= -\frac{1}{i\omega\Lambda}\Delta^{\sigma}_{pqij}\delta(\mathbf{r}) \\ &\quad + \frac{1}{i\omega\rho\Lambda^2}\Delta^{\sigma}_{pqnr}\Delta^{\sigma}_{ijmk}k_n k_m G_{rk}(\mathbf{r}) \qquad (10a)\end{aligned}$$

$$\begin{aligned}G^{+\backslash\sigma,+\backslash\sigma}_{pqij}(\mathbf{r}) &= -\frac{1}{i\omega M}\Delta^{+\backslash\sigma}_{pqij}\delta(\mathbf{r}) \\ &\quad + \frac{1}{i\omega\rho M^2}\Delta^{+\backslash\sigma}_{pqnr}\Delta^{+\backslash\sigma}_{ijmk}k_n k_m G_{rk}(\mathbf{r}) \qquad (10b)\end{aligned}$$

$$G^{\sigma,+\backslash\sigma}_{pqij}(\mathbf{r}) = -\frac{1}{i\omega\rho\Lambda M}\Delta^{\sigma}_{pqnr}\Delta^{+\backslash\sigma}_{ijmk}k_n k_m G_{rk}(\mathbf{r}) \qquad (10c)$$

$$G^{+\backslash\sigma,\sigma}_{pqij}(\mathbf{r}) = -\frac{1}{i\omega\rho\Lambda M}\Delta^{+\backslash\sigma}_{pqnr}\Delta^{\sigma}_{ijmk}k_n k_m G_{rk}(\mathbf{r}) \qquad (10d)$$

$$G^{\sigma,f}_{pqk}(\mathbf{r}) = -\frac{1}{\rho\Lambda}\Delta^{\sigma}_{pqnr}k_n G_{rk}(\mathbf{r}) \qquad (10e)$$

$$G^{+\backslash\sigma,f}_{pqk}(\mathbf{r}) = -\frac{1}{\rho M}\Delta^{+\backslash\sigma}_{pqnr}k_n G_{rk}(\mathbf{r}) \qquad (10f)$$

$$G^{v,\sigma}_{rij}(\mathbf{r}) = -\frac{1}{\rho\Lambda}\Delta^{\sigma}_{ijnk}k_n G_{rk}(\mathbf{r}) \qquad (10g)$$

$$G^{v,+\backslash\sigma}_{rij}(\mathbf{r}) = -\frac{1}{\rho M}\Delta^{+\backslash\sigma}_{ijnk}k_n G_{rk}(\mathbf{r}), \quad G^{v,f}_{rk}(\mathbf{r}) = -\frac{i\omega}{\rho}G_{rk}(\mathbf{r}) \qquad (10h)$$

where

$$G_{rk}(\mathbf{r}) = \frac{1}{v_{\mathrm{S}}^2}\delta_{rk}G_{\mathrm{S}}(\mathbf{r}) + \frac{1}{\omega^2}k_r k_k (G_{\mathrm{P}} - G_{\mathrm{S}})(\mathbf{r}) \qquad (11a)$$

with

$$\begin{aligned}G_{\mathrm{P}}(\mathbf{r}) &= \frac{1}{4\pi|\mathbf{r}|}\exp\left(-\frac{i\omega}{v_{\mathrm{P}}}|\mathbf{r}|\right)\\ G_{\mathrm{S}}(\mathbf{r}) &= \frac{1}{4\pi|\mathbf{r}|}\exp\left(-\frac{i\omega}{v_{\mathrm{S}}}|\mathbf{r}|\right). \qquad (11b)\end{aligned}$$

In (11), $v_{\mathrm{P}} = (\lambda + 2\mu/\rho)^{1/2}$ and $v_{\mathrm{S}} = (\mu/\rho)^{1/2}$ denote the P- and S-wave velocities, respectively.

Based on (4), the scattering wavefield satisfies

$$\begin{bmatrix}-\boldsymbol{\tau}^{\sigma}_{\mathrm{S},pq}\\ -\boldsymbol{\tau}^{+\backslash\sigma}_{\mathrm{S},pq}\\ \mathbf{v}_{\mathrm{S},r}\end{bmatrix} = i\omega\int \begin{bmatrix}\mathbf{G}^{\sigma,\sigma}_{0,pqij} & \mathbf{G}^{\sigma,+\backslash\sigma}_{0,pqij} & \mathbf{G}^{\sigma,f}_{0,pqk}\\ \mathbf{G}^{+\backslash\sigma,\sigma}_{0,pqij} & \mathbf{G}^{+\backslash\sigma,+\backslash\sigma}_{0,pqij} & \mathbf{G}^{+\backslash\sigma,f}_{0,pqk}\\ \mathbf{G}^{v,\sigma}_{0,rij} & \mathbf{G}^{v,+\backslash\sigma}_{0,rij} & \mathbf{G}^{v,f}_{0,rk}\end{bmatrix}\cdot\boldsymbol{\chi}\cdot\begin{bmatrix}\boldsymbol{\tau}^{\sigma}_{ij}\\ \boldsymbol{\tau}^{+\backslash\sigma}_{ij}\\ \mathbf{v}_k\end{bmatrix}d\mathbf{r} \qquad (12)$$

where the property contrast is

$$\boldsymbol{\chi} = \begin{bmatrix}\chi_{\Lambda} & 0 & 0\\ 0 & \chi_M & 0\\ 0 & 0 & \chi_{\rho}\end{bmatrix} \qquad (13a)$$

with

$$\chi_{\Lambda} = \frac{\Lambda}{\Lambda_0} - 1, \quad \chi_M = \frac{M}{M_0} - 1, \quad \chi_{\rho} = \frac{\rho}{\rho_0} - 1. \qquad (13b)$$

In (13), Λ, M, and ρ denote the true properties, and Λ_0, M_0, and ρ_0 denote the parameters of the background model.

Equation (12) can be expressed in the discrete form as

$$\begin{bmatrix}-\boldsymbol{\tau}^{\sigma}_{\mathrm{S},pq}\\ -\boldsymbol{\tau}^{+\backslash\sigma}_{\mathrm{S},pq}\\ \mathbf{v}_{\mathrm{S},r}\end{bmatrix} = i\omega\Delta\mathbf{r}\begin{bmatrix}\mathbf{G}^{\sigma,\sigma}_{0,pqij} & \mathbf{G}^{\sigma,+\backslash\sigma}_{0,pqij} & \mathbf{G}^{\sigma,f}_{0,pqk}\\ \mathbf{G}^{+\backslash\sigma,\sigma}_{0,pqij} & \mathbf{G}^{+\backslash\sigma,+\backslash\sigma}_{0,pqij} & \mathbf{G}^{+\backslash\sigma,f}_{0,pqk}\\ \mathbf{G}^{v,\sigma}_{0,rij} & \mathbf{G}^{v,+\backslash\sigma}_{0,rij} & \mathbf{G}^{v,f}_{0,rk}\end{bmatrix}\begin{bmatrix}\chi_{\Lambda} & 0 & 0\\ 0 & \chi_M & 0\\ 0 & 0 & \chi_{\rho}\end{bmatrix}\begin{bmatrix}\boldsymbol{\tau}^{\sigma}_{ij}\\ \boldsymbol{\tau}^{+\backslash\sigma}_{ij}\\ \mathbf{v}_k\end{bmatrix} \qquad (14)$$

that can be simplified as

$$\mathbf{P}_{\mathrm{S}} = \mathbf{G}\cdot\zeta(\boldsymbol{\chi})\mathbf{P}. \qquad (15)$$

Substituting (15) into (7), we can obtain the Lippmann–Schwinger equation based on the WKBJ approximation

$$\mathbf{P} = \mathbf{P}_0 + \mathbf{G}\cdot\zeta(\boldsymbol{\chi})\mathbf{P} \qquad (16)$$

which can be solved formally as

$$\mathbf{P} = [\mathbf{I} - \mathbf{G}\cdot\zeta(\boldsymbol{\chi})]^{-1}\mathbf{P}_0. \qquad (17)$$

However, a matrix inversion is usually avoided when dealing with large matrices. Approximations, such as Born, are used

TABLE I

FORWARD MODELING ALGORITHM USING THE BORN–WKBJ APPROXIMATION

1. Calculate the incident field $\mathbf{P}_0$ in the absence of any knowledge of the subsurface property contrast $\boldsymbol{\chi}$;
2. According to (19), set up the linear forward operator and update the total field $\mathbf{P}$ by using $\mathbf{P}_0$ and $\boldsymbol{\chi}$;
3. Obtain the scattered wavefield $\mathbf{P}_S$ by (15);
4. Calculate the synthetics by using $\mathbf{P}_S$ according to (20).

to solve this problem. According to this approximation, (16) can be reformulated via a Taylor expansion as

$$\mathbf{P} = \left[\sum_{j=0}^{\infty} (G \cdot \zeta)^j\right] \mathbf{P}_0. \tag{18}$$

Then, by retaining the first-order term, the Born–WKBJ equation of the total wavefield is

$$\mathbf{P} = \mathbf{P}_0 + G\zeta\mathbf{P}_0. \tag{19}$$

The scattered wavefield $\mathbf{P}_\mathrm{S}$ can be obtained. By using the relation between displacement $\mathbf{U}$ and particle velocity $\mathbf{v}$, we obtain

$$\mathbf{v} = i\omega\mathbf{U} \tag{20}$$

from which we can compute the synthetic seismogram by using the scattered wavefield.

The procedure of the forward modeling using Born–WKBJ approximation is indicated in Table I.

B. Inversion Based on the Born–WKBJ Approximation

Equation (7) describes the relationship among the total, the background, and the scattered wave fields

$$\mathbf{P} = \mathbf{P}_0 + \mathbf{P}_\mathrm{S} \tag{21a}$$

with

$$\mathbf{P}_\mathrm{S} = \mathcal{F}(\mathbf{P}) \cdot \boldsymbol{\chi} \tag{21b}$$

where $\mathcal{F}$ denotes a kernel function of $\mathbf{P}$, and $\boldsymbol{\chi}$ is the matrix of the subsurface properties. There is a linear relation between the measured data and the subsurface model.

Based on the regularization algorithm, the objective function of the Born–WKBJ-based inversion is

$$\mathcal{J}(\boldsymbol{\chi}) = \|\mathbf{d}_\mathrm{obs} - \mathcal{F}(\mathbf{P}) \cdot \boldsymbol{\chi}\|_2 + \lambda R(\boldsymbol{\chi}) \tag{22}$$

where $R(\chi)$ denotes the regularization penalty (prior constraint) and λ is a weight coefficient, which balances the data residual and prior constraint. A smaller weight yields a set of sparse solutions, while a larger one causes smoother solutions.

According to (19) and (21), the total wavefield $\mathbf{P}$ is related to the wavefield $\mathbf{P}_0$ of the background model (low-frequency model). Thus, the accuracy of the low-frequency model significantly affects the modeling and inversion results. Then, an effective method for low-frequency model building is required.

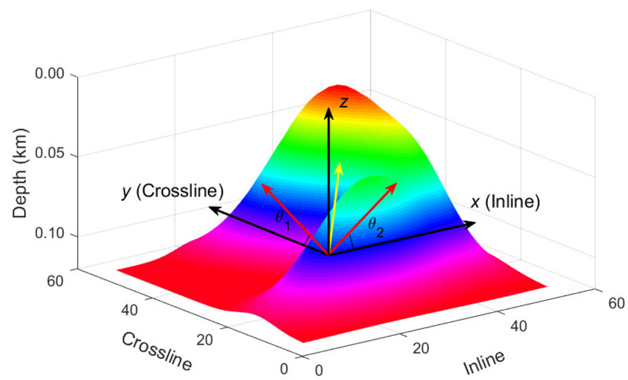

Fig. 1. Diagram showing the relations between 2-D seismic slopes (red arrows in the planes along the inline and crossline directions) with the actual 3-D slope (yellow arrow).

C. 3-D Seismic Slope Attribute Regularized Model Building

It is common to build the low-frequency model by interpolating well logs along the picked geological horizons by artificial interpretation, which requires intensive workloads and considers only a small number of geological elements as constraints, especially for complex structures. Here, a 3-D data-driven model building algorithm is proposed by introducing 3-D seismic slope attributes of geological structures as interpolation constraints. According to Huang *et al.* [44], one can achieve the models by interpolating well logs with 2-D seismic slopes. Such slope attributes, extracted from seismic profiles by a plane-wave decomposition algorithm, are used to replace the artificially picked horizons as lateral constraints. However, this method is 2-D by using 2-D slope estimation and 2-D interpolation algorithm.

Fig. 1 shows a 3-D model with structural features. The yellow arrow shows the true slope direction of a point example and can be computed by two 2-D slope directions (red arrows) in x (inline) and y (crossline) planes with the angles θ_2 and θ_1 with respect to the x- and y-axes, respectively. Then, the slope at this point is

$$\theta = \arccos(\cos\theta_1 \cos\theta_2) \tag{23}$$

where θ_2 and θ_1 denote the seismic slope attributes along the inline and crossline directions, respectively, which can be calculated by the 3-D PWD algorithm (see Appendix).

By considering the extracted slope attributes as lateral constraints, an interpolation strategy is presented by solving the inverse problem to reconstruct the 3-D models of the subsurface properties.

Fig. 2 shows the equivalent of a field example (square area) with several randomly distributed wells (small circles). By taking the well marked by the red solid circle as a reference, the 2-D geological-structure-guided model building [44] performs the interpolation along the inline or crossline directions with a 2-D slope attribute. However, the process is more complex in the 3-D case, since we have to interpolate in arbitrary directions. Let us assume that we need to reconstruct a 3-D model by using the reference well (red solid circle). With this well at the center of a circle, rotating the interpolation direction through a certain angle, we have the 2-D profile

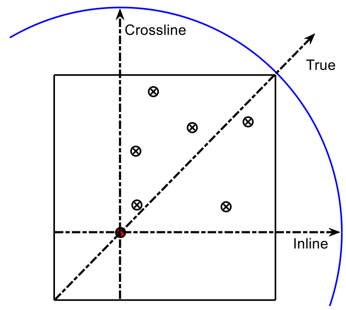

Fig. 2. Diagram showing the well-log data interpolation by using the 3-D seismic slope attribute.

along the "true" direction indicated by the oblique dashed line in Fig. 2. Then, we obtain the 3-D seismic slope θ by using (23) and the 3-D PWD outlined in the Appendix. Based on this slope, the 2-D interpolation along the "true" profile can be performed by solving a shaping-regularization-based inverse problem. Then, continuing the rotation of the "true" direction, we perform the same operation until we cover the complete circle. And the final 3-D model is obtained by resampling all the 2-D interpolated profiles according to the grids of the field.

Next, the geological-structure-guided interpolation process is explained. Generally, the wells are randomly distributed in a real field and can be considered as a sampling (or mask) operator to act on a subsurface property model

$$\mathbf{\Psi}\mathbf{X} = \mathbf{Y}_{\text{log}} \tag{24}$$

where $\mathbf{\Psi}$ denotes the matrix of the sampling operator, $\mathbf{X}$ corresponds to the subsurface property model, and $\mathbf{Y}_{\text{log}}$ represents the sparsely distributed well logs. Due to the sparsity sampling, most of the components of the sampling operator are zero. Thus, the inverse problem in (24) is ill-posed. Regularization is one of the most widely used methods to solve this problem. The conventional L_2-norm regularized misfit function is

$$\hat{\mathbf{X}} = \arg\min \left\| \mathbf{\Psi}\mathbf{X} - \mathbf{Y}_{\text{log}} \right\|_2^2 + \lambda \|\mathbf{X}\|_2^2. \tag{25}$$

However, the model building process solved by (24) is not constrained by seismic data, and the inclusion of geological information as a lateral constraint is necessary. Therefore, an objective function based on a reshaping regularization is built, which introduces the slope attributes as constraints to solve the inverse problem, instead of the classical interpolation to obtain the reconstructed models. In this framework, a structural smoothing operator [45], [46] is introduced and the problem is iteratively solve as

$$\hat{\mathbf{X}} = \left(\mathbf{I} - \mathbf{S} + \lambda\mathbf{S}\mathbf{\Psi}^{\mathrm{T}}\mathbf{\Psi}\right)^{-1} \cdot \lambda\mathbf{S}\mathbf{\Psi}^{\mathrm{T}}\mathbf{Y}_{\text{log}} \tag{26}$$

where $\mathbf{S}$ and $\mathbf{\Psi}^{\mathrm{T}}$ denote the shaping operator and the adjoint of the forward operator, respectively. The structural smoothness shaping operator $\mathbf{S}$ is

$$\mathbf{S} = \mathbf{P}\mathbf{H}\mathbf{H}^{\mathrm{T}}\mathbf{P}^{\mathrm{T}} \tag{27}$$

where $\mathbf{H}$ is a triangle smoothing operator according to Chen *et al.* [43] and Fomel [45], [46] and $\mathbf{P}$ is a summation operator to average all the traces along the structural direction. Setting $\lambda = 1/c^2$ and substituting (27) into (26), we obtain

$$\hat{\mathbf{X}} = \mathbf{P}\mathbf{H}\left[c^2\mathbf{I} + \mathbf{H}^{\mathrm{T}}\mathbf{P}^{\mathrm{T}}\left(\mathbf{\Psi}^{\mathrm{T}}\mathbf{\Psi} - c^2\mathbf{I}\right)\mathbf{P}\mathbf{H}\right]^{-1}\mathbf{H}^{\mathrm{T}}\mathbf{P}^{\mathrm{T}}\mathbf{\Psi}^{\mathrm{T}}\mathbf{Y}_{\text{log}}. \tag{28}$$

In (28), $\hat{\mathbf{X}}$ denotes the interpolated 2-D model. Unlike the classical Tikhonov regularization, the shaping regularization iterative algorithm introduces the geological structure constraint from seismic data by using a structural smoothness shaping operator $\mathbf{S}$. In building an initial model, a slope attribute extracted by the PWD algorithm is set to define $\mathbf{S}$. Table II outlines the algorithm for the 3-D model building method.

TABLE II

ALGORITHM OUTLINING THE MODEL BUILDING METHOD BASED ON THE 3-D SEISMIC SLOPES

1. Input: Post-stack seismic data and well logs $\mathbf{Y}_{log}$;
2. Lateral constraint:
2-1. Extract 2-D slope attributes from seismic data by using the PWD algorithm (see Appendix) along the inline and crossline directions;
2-2. Calculate the 3-D slope attributes based on 2-D slopes according to equation (23);
3. Inversion-based interpolation:
3-1. Set a reference well as the center of a circle, and perform rotations to define the target direction;
3-2. Perform the 2-D interpolation along this direction:
a. Build the shaping operator $\mathbf{S}$ by using the slope obtained in 2-2
b. Solve the shaping regularized inversion according to (28) and start the inversion loop: j=1, 2, 3, ..., $j_{\max}$
c. Obtain the 2-D interpolated model $\mathbf{X}$;
3-3. Continue the rotation until all the 2-D interpolated models are obtained covering the complete circle;
5. Resampling: Resample all the 2-D interpolated models to get the 3-D model;
6. Output: 3-D interpolated models
7. Post processing: Extract the reliable low-frequency information from the interpolated 3-D models as the background models for the forward modeling and the initial models for the inversion.

III. EXAMPLES

A. Born–WKBJ Approximation Modeling

We use a 1-D model to analyze how the Born–WKBJ-approximation forward modeling is affected by the low-frequency background model. The 1-D profile is part of the Marmousi model [48], [49], as shown in Fig. 3(a), which shows the elastic properties v_{P}, v_{S}, and ρ, and Λ and M obtained with (6), while (13) gives χ_Λ, χ_M, and χ_ρ [see Fig. 3(b)]. These logs (blue curves) are considered as the true properties, and we use different low-frequency models to analyze the influence of the background model on the synthetic responses computed with the Born–WKBJ approximation.

Travel times are highly affected by the low-frequency (long-wavelength) component of the model. And inaccurate velocity

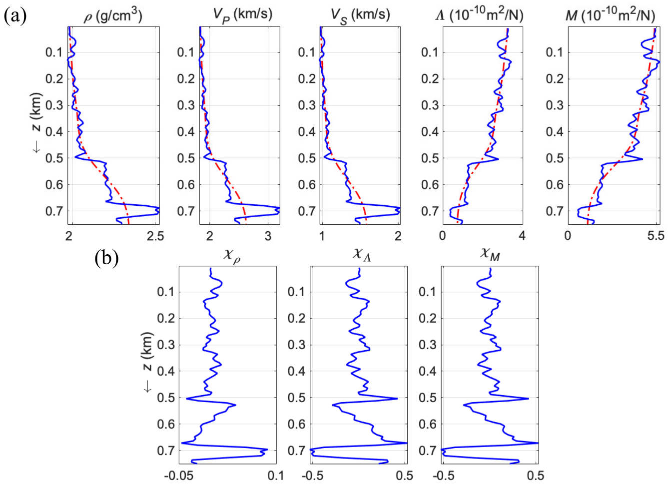

Fig. 3. (a) Elastic properties v_P, v_S, ρ, Λ, and M of a trace extracted from the Marmousi model, where the blue and red lines denote the real and low-frequency background models, respectively. (b) Contrast parameters χ_Λ, χ_M, and χ_ρ calculated by using properties in (a).

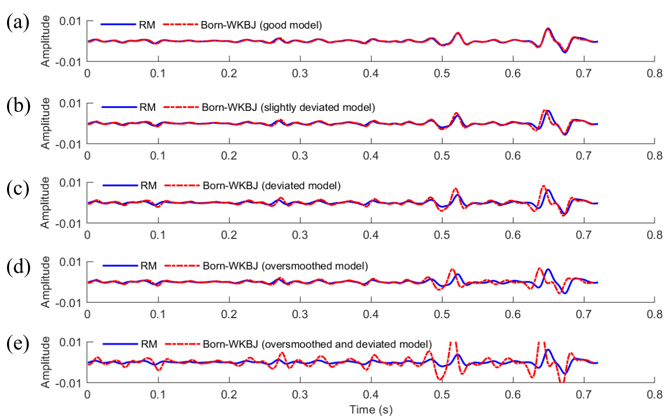

Fig. 4. Zero-offset synthetic seismic traces obtained with the reflectivity method (blue solid curves) and Born–WKBJ approximation by using different background models (red-dashed curves). (a) Good. (b) Slightly deviated. (c) Deviated. (d) Oversmoothed. (e) Oversmoothed and deviated models.

information can cause a travel time gap between the synthetic and the observed data, which may even lead to the cycle-skipping phenomenon [19].

Fig. 4 shows zero-offset synthetic traces (red-dashed curves) obtained with the Born–WKBJ approximation for different low-frequency background models. From top to bottom, the synthetic data (red-dashed) are simulated with the true, the slightly deviated (only a few samples deviated from the true ones), the moderately deviated (a part of samples deviated from the true ones), the over-smoothed, and the poor (over-smoothed and partially deviated) models, respectively. The reflectivity method (RM, blue curves in Fig. 4) is used as a benchmark for comparison. The comparison indicates that deviations from the true model affect the travel times and the amplitudes depending on the magnitude of the deviation. The slightly deviated model achieves the response with the relatively exact travel time and amplitudes [see Fig. 4(b)]. The over-smoothed model lacking important structural information leads to a significant difference of travel time between the

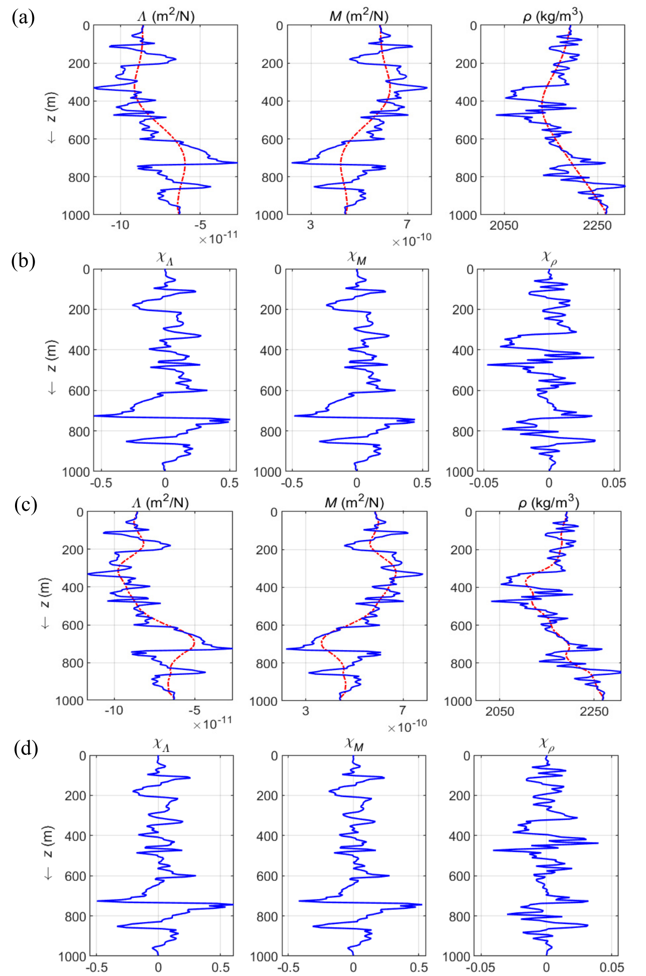

Fig. 5. (a) and (c) Well-log profiles (blue) and background models (red). (b) and (d) Contrast parameters obtained with the true logs and the background models. (a) and (b) Over-smoothed. (c) and (d) Regular models.

Born–WKBJ and exact simulations [see Fig. 4(d)]. When the time shift exceeds half a wavelength, the cycle skipping phenomenon occurs, which poses serious problems for the wave-equation-based inversion process. When using the over-smoothed model with many wrong samples, we can see the serious deviations of the waveform [see Fig. 4(e)]. Thus, a suitable background model is essential for the accuracy of wavefield simulation by Born–WKBJ approximation method. The proposed model building based on 3-D slope attributes provides a reasonable background model to obtain accurate synthetic traces. Besides, it gives an initial model with good low-frequency information for gradient-based seismic inversions.

B. Born–WKBJ Inversion

To further verify the effect of a given low-frequency model on the Born–WKBJ inversion, we adopt a well-log model, including logs of Λ, M, and ρ, shown as blue lines in Fig. 5(a) and (c). By smoothing these logs, we obtain two kinds of initial models, an over-smoothed version [red lines in Fig. 5(a)] and a relatively regular one [red lines in Fig. 5(c)] as background for simulation and initial models for inversion. Fig. 5(b) and (d) shows χ_Λ, χ_M, and χ_ρ computed with (13),

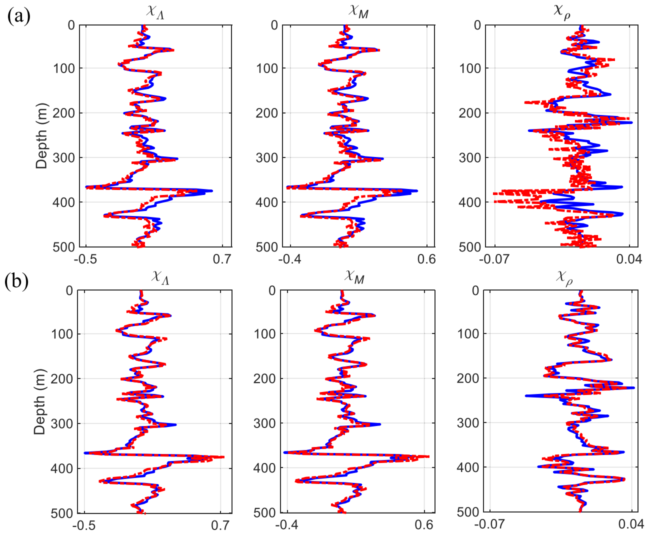

Fig. 6. True model (blue) and inversion (red) by using (a) over-smoothed model of Fig. 5(b) and (b) regular (better) model of Fig. 5(d).

using the over-smoothed [see Fig. 5(a)] and regular models [see Fig. 5(c)]. We generate a pre-stack angle gather by convolving the reflection coefficients with a Ricker wavelet of 30-Hz dominant frequency.

Then, by using the pre-stack inversion based on the Born–WKBJ approximation, we obtain the inverted χ_Λ, χ_M, and χ_ρ. As shown in Fig. 6, the initial model significantly affects the results. Compared with the over-smoothed model, the regular one yield better results [see Fig. 6(b)]. The results of the over-smoothed model show significant deviations from the true model, especially the density [right panel in Fig. 6(a)].The numerical example verifies the importance of a good low-frequency initial model to the Born–WKBJ pre-stack inversion. To obtain a reasonable initial model with a suitable low-frequency trend, we introduce the proposed 3-D geological-structure-guided model building in Section III-C.

Gaussian random noise is added to the synthetic data to obtain gathers with SNR (signal-noise-ratio) of 10, 5, and 2, which are used to verify the stability of the Born–WKBJ method. Fig. 7 shows the results, where the regular initial models of Fig. 5(d) are adopted. The root-mean-square errors (RMSE) between the inversion and real data are given in Table III. Fig. 7(a) shows that the inversion using the gather with an SNR of 10 agrees well with the true one (blue lines). For an SNR of 5, the velocities are still acceptable, but the inverted density has more errors (see Table III). The results with an SNR of 2 [see Fig. 7(c)] indicate that the density is more affected by noise than the velocities.

The Born–WKBJ method is compared with the conventional method, that is, the Zoeppritz-based least-squares inversion. Here, a multilayer block model is set up in the depth domain [see the blue lines in Fig. 8(b)]. The input gather is generated by the Born–WKBJ approximation, which includes the full-wavefield. Fig. 8 shows the comparison between the conventional method and the Born–WKBJ waveform inversion in the time (a) and depth (b) domains. Since the former does not consider the full wave response, the results are unacceptable,

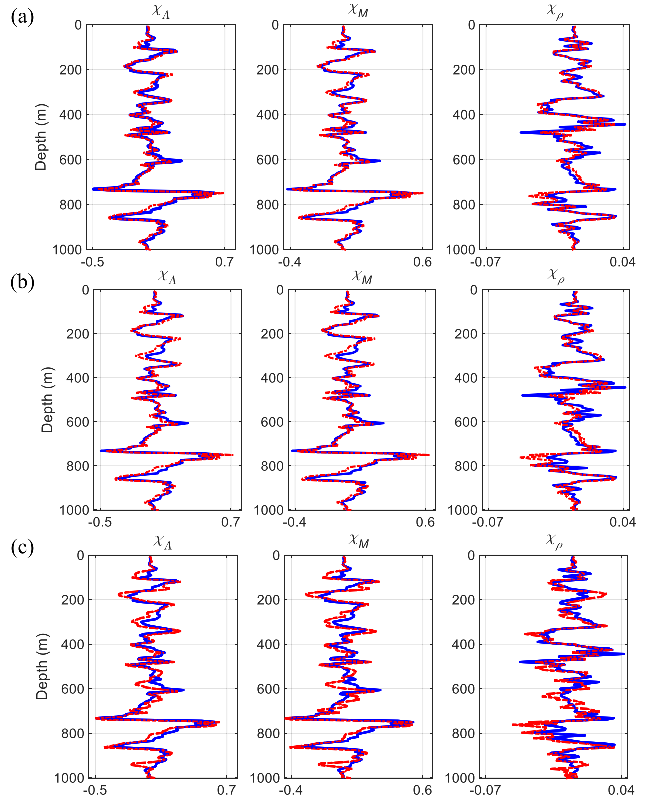

Fig. 7. Born–WKBJ inversion using gathers with SNR of (a) 10, (b) 5, and (c) 2. The real data and inversion results are indicated with blue solid and red dashed lines, respectively.

TABLE III

Root-Mean-Square Errors (RMSE) Between the Inversion Results in Fig. 7 and the Real Data

RMSE	χ_Λ	χ_M	χ_ρ
SNR=10	0.3214	0.3382	0.1491
SNR=5	0.3566	0.3717	0.3201
SNR=2	0.4612	0.4890	0.7496

especially for the density, where the multiples and converted modes of the input data, regarded as primary reflections, are a cause of errors [see Fig. 8(a)]. In contrast, the Born–WKBJ method makes use of the various internal multiple reflections and obtains better results [see Fig. 8(b)].

C. 3-D Structural-Geology Model Building

Clarbout's "qdome" model [50] is considered as an example to test the model building method. Fig. 9 shows the 3-D cube and inner profiles of the "qdome" v_P model. It has a complex geological structure, which is difficult to manually pick and generate an initial model. The proposed approach builds the 3-D model as the following steps.

1) As shown in Fig. 10(a), a depth-domain seismic data, or seismic image, is obtained with the root-mean-square velocity, using time-depth conversion.
2) We extract two plane-wave slope attributes in the inline [see Fig. 11(a)] and crossline [see Fig. 11(b)] directions

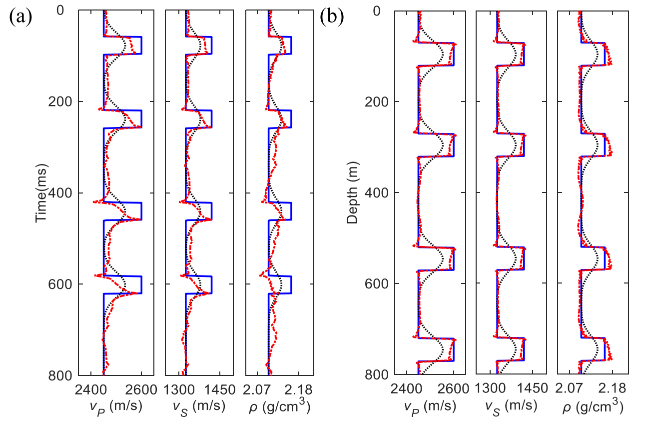

Fig. 8. Inversion results of a block model using a gather with the full wave responses. (a) Time domain by Zoeppritz-based AVA inversion. (b) Depth domain by Born–WKBJ waveform inversion. The blue solid, black dotted, and red dashed line are the real data, initial, and inverted models, respectively.

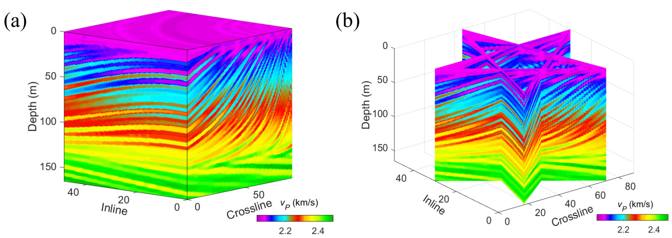

Fig. 9. 3-D Claerbout's "qdome" P-wave velocity v_P model. (a) 3-D cube. (b) Inner details.

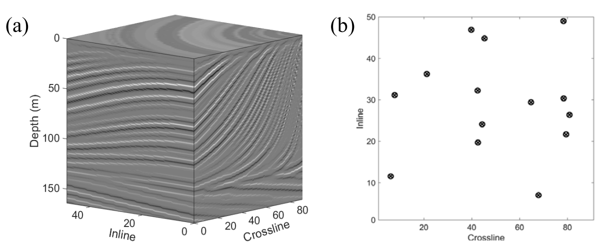

Fig. 10. (a) 3-D post-stack seismic data of the "qdome" model and (b) random well locations on the base map.

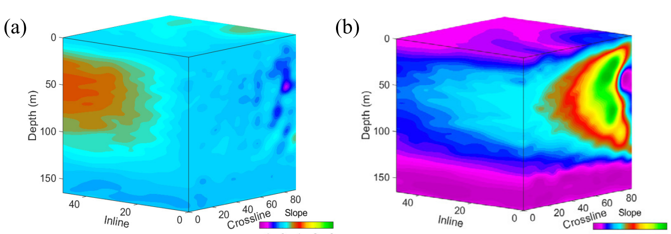

Fig. 11. Seismic slope attributes, extracted from Fig. 10(a), along (a) inline and (b) crossline directions, by using the 3-D PWD algorithm.

from the depth-domain data by using the 3-D PWD algorithm (see the Appendix).

3) Randomly distributed well-log locations are displayed in the base map [see Fig. 10(b)]. From well-log data and the seismic slope attributes, we obtain the interpolated model (see Fig. 12) according to the process in Table II.

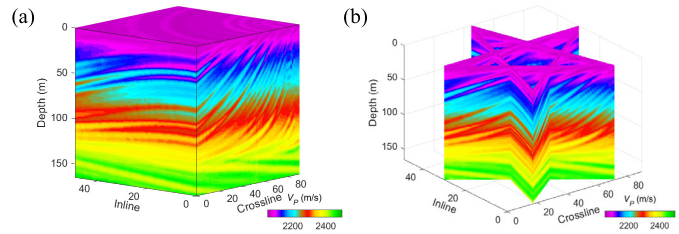

Fig. 12. Interpolated model by using the 3-D model building algorithm. (a) 3-D cube. (b) Inner details.

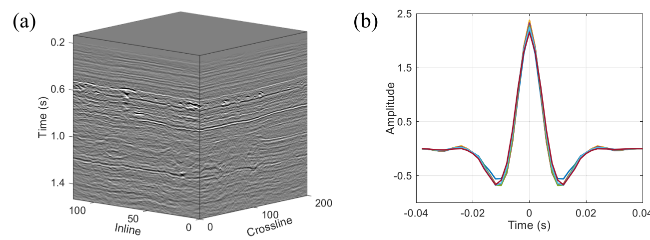

Fig. 13. (a) 3-D post-stack seismic data and (b) wavelets extracted from the angle gathers.

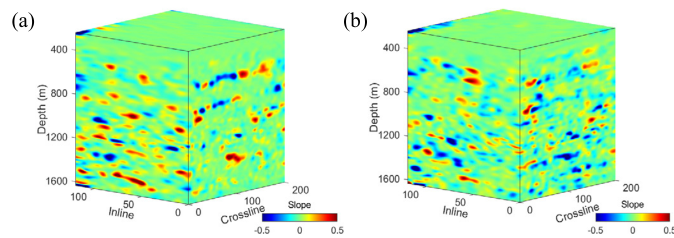

Fig. 14. Seismic slope attributes extracted from the 3-D data in Fig. 13(a) along (a) inline and (b) crossline directions.

Comparing the interpolated (see Fig. 12) and the actual model (see Fig. 9), we find that the proposed method can effectively restore the real model. At least, it provides a proper low-frequency trend.

IV. Real-Data Application

Seismic data from an oilfield in the North Sea is used to verify the feasibility of the proposed 3-D model building and Born–WKBJ inversion. Fig. 13(a) shows the 3-D post-stack seismic data, which contains 121 survey lines, each with 201 CDPs. The angle of the pre-stack gathers ranges from 0° to 30°. As shown, the target section has a relatively stable geological structure, which is suitable for the scattering integral equation (Born–WKBJ approximation) as forward modeling. The seismic wavelets used for inversion are extracted from the angle gathers, including the wavelets for near-, mid-, and far-angle, as shown in Fig. 13(b). The available logs are P- (v_P) and S-wave (v_S) velocities, and density (ρ).

The 3-D geological-structure-guided model building is adopted to compute the background models of the forward modeling and the initial models for the inversion. We extract seismic slope attributes by using the 3-D PWD algorithm from the post-stack data (see Appendix). Fig. 14(a) and (b) shows the slope cubes along the inline and crossline directions, respectively. Setting the seismic slopes as constraints,

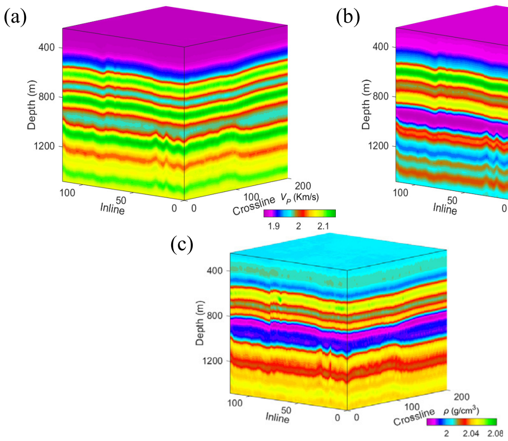

Fig. 15. Low-frequency background models by using the proposed 3-D model building. (a) v_P. (b) v_S. (c) ρ.

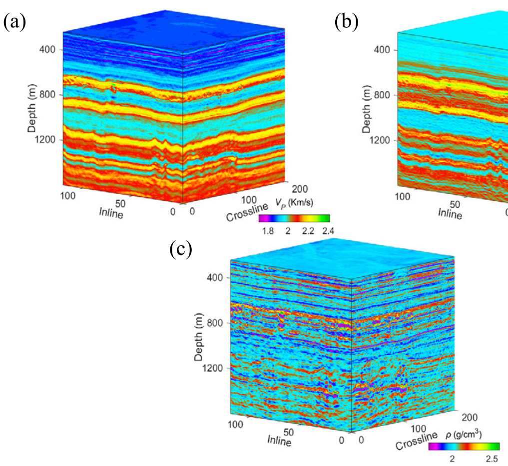

Fig. 16. 3-D inversion by using Born–WKBJ approximation, based on the over-smoothed model. (a) v_P. (b) v_S. (c) ρ.

we interpolate the well-log data by using an inversion method based on the shaping regularization and obtain the 3-D low-frequency models, as shown in Fig. 15, which shows the low-frequency models of v_P [see Fig. 15(a)], v_S [see Fig. 15(b)], and ρ [see Fig. 15(c)]. Regarding the Born–WKBJ inversion, the target parameters are the contrasts of the elastic parameters χ_Λ, χ_M, and χ_ρ, which are computed according to (13).

We perform the inversion to obtain the contrasts using two sets of initial models, the over-smoothed model (obtained by smoothing the models in Fig. 15) and the regular model, built with the proposed method (shown in Fig. 15). Figs. 16 and 17 show the results of the inversion based on the over-smoothed and regular models, respectively, where the differences are evident, with the latter results much better (containing more detailed information). The results of the over-smoothed model show a lower resolution and contain scarce high-frequency information, especially for v_P and v_S. The results for density are the worst, but the improvement of the continuity in density by using the regular model can be observed in the deeper formations. Density is much less sensitive to seismic response than velocity, and it is difficult with conventional PP

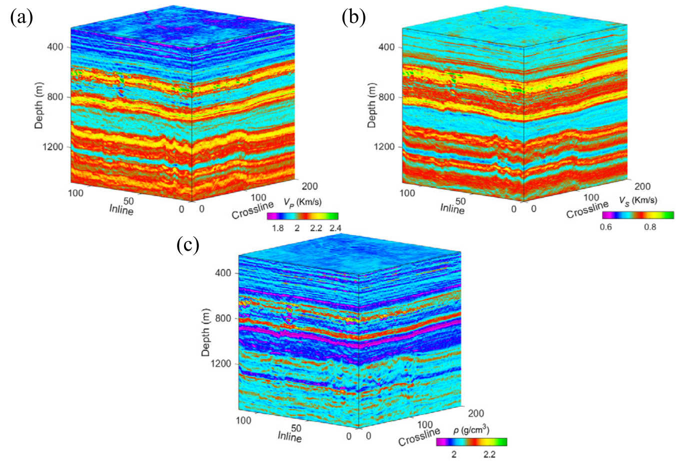

Fig. 17. 3-D inverted by using Born–WKBJ approximation, based on the regular model. (a) v_P. (b) v_S. (c) ρ.

inversion methods, using wave equation inversion, to obtain an acceptable density estimation. Here, the far-angle range of the seismic data is not used for the inversion test due to the bad quality, which maybe another reason for the unexpected density estimations.

V. Conclusion

We implement a 3-D geological-structure-guided model building into a pre-stack seismic inversion based on the Born–WKBJ approximation. Unlike other forward operators, for example, the reflectivity method, the modeling accuracy depends strongly on a proper background (low-frequency) model, which can be obtained with the present model building algorithm. Besides, the methodology provides a suitable initial model for the gradient-based inversion. Synthetic and real-data applications demonstrate that the inversion combined the proposed model building algorithm provides acceptable results for subsurface-property characterization.

Appendix

3-D Plane-Wave Destruction

According to Claerbout [51], local plane waves can be expressed by the following differential equation:

$$\frac{\partial \mathbf{P}}{\partial x} + \theta \frac{\partial \mathbf{P}}{\partial t} = 0 \tag{A.1}$$

where θ is the seismic slope attribute and $\mathbf{P}$ denotes the wavefield data which is a function of time (t) and space (x). In a local area, the slope can be considered as a constant, thus

$$\mathbf{P}(x, t) = f(t - \theta x). \tag{A.2}$$

Transforming (A.1) from the time to frequency domain yields

$$\frac{\partial \hat{\mathbf{P}}}{\partial x} + i\omega\theta\hat{\mathbf{P}} = 0 \tag{A.3}$$

where $\hat{\mathbf{P}}$ is the frequency-space version of $\mathbf{P}$ obeying

$$\hat{\mathbf{P}}(x) = \hat{\mathbf{P}}(0)e^{i\omega\theta x} \tag{A.4}$$

which means that a plane wave can be predicted by a two-term filter. In other words, several plane waves can be accomplished by cascading several filters. The filter can be represented in the Z transform as

$$A(Z_x) = 1 + a_1 Z_x + a_2 Z_x^2 + \cdots + a_N Z_x^N \tag{A.5}$$

or

$$A(Z_x) = \left(1 - \frac{Z_x}{Z_1}\right)\left(1 - \frac{Z_x}{Z_2}\right)\cdots\left(1 - \frac{Z_x}{Z_N}\right) \tag{A.6}$$

where Z_i corresponds to the zero points of the polynomial. The 2-D filter in the time-space domain can be expressed as

$$A(Z_t, Z_x) = 1 - Z_x \frac{B(Z_t)}{B(1/Z_t)}. \tag{A.7}$$

The ratio $B(Z_t)/B(1/Z_t)$ denotes an all-pass digital filter approximating the time-shift operator $e^{i\omega\theta}$. According to Fomel [45], we define a modified form of the filter in (A.6) as

$$C(Z_t, Z_x) = A(Z_t, Z_x)B\left(\frac{1}{Z_t}\right) = B\left(\frac{1}{Z_t}\right) - Z_x B(Z_t) \tag{A.8}$$

which avoids the polynomial division. The plane-wave destruction filter C is a function of the slope attribute θ. When expanding the 2-D condition to 3-D, we need to estimate two different slopes θ_1 and θ_2 from the available data simultaneously. According to Fomel [45], one can update the initial slopes by using $\Delta\theta_1$ and $\Delta\theta_2$ after solving the following linear equation:

$$\mathbf{C}'(\theta_1)\mathbf{C}(\theta_2)\Delta\theta_1\mathbf{d} + \mathbf{C}(\theta_1)\mathbf{C}'(\theta_2)\Delta\theta_2\mathbf{d} + \mathbf{C}(\theta_1)\mathbf{C}(\theta_2)\mathbf{d} \approx 0. \tag{A.9}$$

Here, $\mathbf{C}(\theta)$ denotes an operator of convolving the known data $\mathbf{d}$ with the filter $C(Z_t, Z_x)$ in (A.7), and differentiating the filter operator $\mathbf{C}(\theta)$ with respect to θ, we obtain $\mathbf{C}'(\theta)$. The regularization should be applied to both slopes along the two dimension θ_1 and θ_2:

$$\varepsilon\mathbf{D}\Delta\theta_1 \approx 0, \quad \varepsilon\mathbf{D}\Delta\theta_2 \approx 0 \tag{A.10}$$

where D and ε denote an appropriate roughening operator and a scaling coefficient, respectively.

Then the seismic slopes θ_1 and θ_2 for the 3-D case are obtained.

REFERENCES

[1] C. Luo, J. Ba, J. M. Carcione, G. Huang, and Q. Guo, "Joint PP and PS pre-stack seismic inversion for stratified models based on the propagator matrix forward engine," *Surv. Geophys.*, vol. 41, no. 5, pp. 987–1028, Sep. 2020.

[2] R.-E. Plessix, "A review of the adjoint-state method for computing the gradient of a functional with geophysical applications," *Geophys. J. Int.*, vol. 167, no. 2, pp. 495–503, Nov. 2006.

[3] G. Huang, X. Chen, C. Luo, and X. Li, "Prestack waveform inversion by using an optimized linear inversion scheme," *IEEE Trans. Geosci. Remote Sens.*, vol. 57, no. 8, pp. 5716–5728, Aug. 2019.

[4] C. Luo, X. Li, and G. Huang, "Pre-stack AVA inversion by using propagator matrix forward modeling," *Pure Appl. Geophys.*, vol. 176, no. 10, pp. 4445–4476, Oct. 2019.

[5] M. K. Sen and P. L. Stoffa, "Nonlinear one-dimensional seismic waveform inversion using simulated annealing," *Geophysics*, vol. 56, no. 10, pp. 1624–1638, 1991.

[6] G. Huang, X. Chen, C. Luo, and Y. Chen, "Mesoscopic wave-induced fluid flow effect extraction by using frequency-dependent prestack waveform inversion," *IEEE Trans. Geosci. Remote Sens.*, vol. 59, no. 8, pp. 6510–6524, Aug. 2021, doi: 10.1109/TGRS.2020.3028032.

[7] C. Luo, G. Huang, X. Chen, and Y. Chen, "Registration-free multicomponent joint AVA inversion using optimal transport," *IEEE Trans. Geosci. Remote Sens.*, early access, Mar. 18, 2021, doi: 10.1109/TGRS.2021.3063271.

[8] A. Buland and H. Omre, "Bayesian linearized AVO inversion," *Geophysics*, vol. 68, no. 1, pp. 185–198, Jan. 2003.

[9] W. Alemie and M. D. Sacchi, "High-resolution three-term AVO inversion by means of a Trivariate Cauchy probability distribution," *Geophysics*, vol. 76, no. 3, pp. R43–R55, May 2011.

[10] Q. Guo, J. Ba, C. Luo, and S. Xiao, "Stability-enhanced prestack seismic inversion using hybrid orthogonal learning particle swarm optimization," *J. Petroleum Sci. Eng.*, vol. 192, Sep. 2020, Art. no. 107313.

[11] Q. Guo, J. Ba, and C. Luo, "Prestack seismic inversion with data-driven MRF-based regularization," *IEEE Trans. Geosci. Remote Sens.*, vol. 59, no. 8, pp. 7122–7136, Aug. 2021, doi: 10.1109/TGRS.2020.3019715.

[12] G. Huang, X. Chen, C. Luo, and Y. Chen, "Pre-stack seismic inversion based on-norm regularized logarithmic absolute misfit function," *Geophys. Prospecting*, vol. 68, no. 8, pp. 2419–2443, Oct. 2020, doi: 10.1111/1365-2478.13012.

[13] S. Mallick, "Amplitude-variation-with-offset, elastic-impedence, and wave-equation synthetics—A modeling study," *Geophysics*, vol. 72, no. 1, pp. C1–C7, Jan. 2007.

[14] T. Li and S. Mallick, "Multicomponent, multi-azimuth pre-stack seismic waveform inversion for azimuthally anisotropic media using a parallel and computationally efficient non-dominated sorting genetic algorithm," *Geophys. J. Int.*, vol. 200, no. 2, pp. 1136–1154, 2015.

[15] H. Liu, J. Li, X. Chen, B. Hou, and L. Chen, "Amplitude variation with offset inversion using the reflectivity method," *Geophysics*, vol. 81, no. 4, pp. R185–R195, Jul. 2016.

[16] A. Tarantola, "Inversion of seismic reflection data in the acoustic approximation," *Geophysics*, vol. 49, no. 8, pp. 1259–1266, 1984.

[17] A. Tarantola, "A strategy for nonlinear elastic inversion of seismic reflection data," *Geophysics*, vol. 51, no. 10, pp. 1893–1903, 1986.

[18] C. Luo, J. Ba, J. M. Carcione, G. Huang, and Q. Guo, "Joint PP and PS pre-stack AVA inversion for VTI medium based on the exact graebner equation," *J. Petroleum Sci. Eng.*, vol. 194, Nov. 2020, Art. no. 107416.

[19] L. Métivier, R. Brossier, Q. Mérigot, E. Oudet, and J. Virieux, "Measuring the misfit between seismograms using an optimal transport distance: Application to full waveform inversion," *Geophys. J. Int.*, vol. 205, no. 1, pp. 345–377, 2016.

[20] S. Mallick and L. N. Frazer, "Practical aspects of reflectivity modeling," *Geophysics*, vol. 52, no. 10, pp. 1355–1364, 1987.

[21] D. Tetyukhina, S. M. Luthi, and D. Gisolf, "Acoustic nonlinear full-waveform inversion on an outcrop-based detailed geological and petrophysical model (Book cliffs, Utah)," *AAPG Bull.*, vol. 98, no. 1, pp. 119–134, Jan. 2014.

[22] N. Portzgen, D. Gisolf, and D. J. Verschuur, "Wave equation-based imaging of mode converted waves in ultrasonic NDI, with suppressed leakage from nonmode converted waves," *IEEE Trans. Ultrason., Ferroelectr., Freq. Control*, vol. 55, no. 8, pp. 1768–1780, Aug. 2008.

[23] G. Rizzuti and A. Gisolf, "An iterative method for 2D inverse scattering problems by alternating reconstruction of medium properties and wavefields: Theory and application to the inversion of elastic waveforms," *Inverse Problems*, vol. 33, no. 3, Mar. 2017, Art. no. 035003.

[24] R. W. Clayton and R. H. Stolt, "A Born-WKBJ inversion method for acoustic reflection data," *Geophysics*, vol. 46, no. 11, pp. 1559–1567, Nov. 1981.

[25] L. Liang, A. Abubakar, and T. M. Habashy, "Reservoir property mapping and monitoring from joint inversion of time-lapse seismic, electromagnetic, and production data," *Geophysics*, vol. 81, no. 5, pp. ID73–ID84, Sep. 2016.

[26] G. L. Wang and A. Abubakar, "Rapid simulation of borehole electromagnetic response in axially symmetric and transversely isotropic formations," *Geophysics*, vol. 83, no. 4, pp. E245–E257, Jul. 2018.

[27] S. Raz, "Three-dimensional velocity profile inversion from finite-offset scattering data," *Geophysics*, vol. 46, no. 6, pp. 837–842, Jun. 1981.

[28] R. Snieder, *General Theory of Elastic Wave Scattering*. Amsterdam, The Netherlands: Elsevier, 2002.

[29] A. Abubakar and P. M. van den Berg, "The contrast source inversion method for location and shape reconstructions," *Inverse Problems*, vol. 18, no. 2, p. 495, 2002.

[30] A. Abubakar and P. M. van den Berg, "Iterative forward and inverse algorithms based on domain integral equations for three-dimensional electric and magnetic objects," *J. Comput. Phys.*, vol. 195, no. 1, pp. 236–262, 2004.

[31] A. Abubakar, P. M. van den Berg, and S. Y. Semenov, "A robust iterative method for Born inversion," *IEEE Trans. Geosci. Remote Sens.*, vol. 42, no. 2, pp. 342–354, Feb. 2004.

[32] X. Huang, M. Jakobsen, and R.-S. Wu, "On the applicability of a renormalized born series for seismic wavefield modelling in strongly scattering media," *J. Geophys. Eng.*, vol. 17, no. 2, pp. 277–299, Apr. 2020.

[33] M. Jakobsen, X. Huang, and R.-S. Wu, "Homotopy analysis of the Lippmann–Schwinger equation for seismic wavefield modelling in strongly scattering media," *Geophys. J. Int.*, vol. 222, no. 2, pp. 743–753, Aug. 2020.

[34] L.-Y. Fu, "Rough surface scattering: Comparison of various approximation theories for 2D SH waves," *Bull. Seismol. Soc. Amer.*, vol. 95, no. 2, pp. 646–663, Apr. 2005.

[35] S. Hu, L.-Y. Fu, and Z. Yao, "Comparison of various approximation theories for randomly rough surface scattering," *Wave Motion*, vol. 46, no. 5, pp. 281–292, Aug. 2009.

[36] X. Song, M. Li, F. Yang, S. Xu, and A. Abubakar, "Three-dimensional joint inversion of EM and acoustic data based on contrast source inversion," *IEEE J. Multiscale Multiphys. Comput. Tech.*, vol. 5, pp. 28–36, 2020.

[37] J. Yang, A. Abubakar, P. M. van den Berg, T. M. Habashy, and F. Reitich, "A CG-FFT approach to the solution of a stress-velocity formulation of three-dimensional elastic scattering problems," *J. Comput. Phys.*, vol. 227, no. 24, pp. 10018–10039, Dec. 2008.

[38] J. Yang and A. Abubakar, "A contrast-source integral-equation approach for three-dimensional modeling of elastic wave problems," *Wave Motion*, vol. 49, no. 7, pp. 638–658, Nov. 2012.

[39] S. Gan, S. Wang, Y. Chen, S. Qu, and S. Zu, "Velocity analysis of simultaneous-source data using high-resolution semblance—Coping with the strong noise," *Geophys. J. Int.*, vol. 204, no. 2, pp. 768–779, Feb. 2016.

[40] X. Zhu, D. P. Sixta, and B. G. Angstman, "Tomostatics: Turning-ray tomography static corrections," *Lead. Edge*, vol. 11, no. 12, pp. 15–23, 1992.

[41] C. A. Zelt and P. J. Barton, "Three-dimensional seismic refraction tomography: A comparison of two methods applied to data from the Faeroe Basin," *J. Geophys. Res., Solid Earth*, vol. 103, no. B4, pp. 7187–7210, Apr. 1998.

[42] J. Korenaga *et al.*, "Crustal structure of the southeast Greenland margin from joint refraction and reflection seismic tomography," *J. Geophys. Res., Solid Earth*, vol. 105, p. 21 591-21 614, 2000.

[43] Y. Chen, H. Chen, K. Xiang, and X. Chen, "Geological structure guided well log interpolation for high-fidelity full waveform inversion," *Geophys. J. Int.*, vol. 207, no. 2, pp. 1313–1331, 2016.

[44] G. Huang, X. Chen, C. Luo, and Y. Chen, "Geological structure-guided initial model building for prestack AVO/AVA inversion," *IEEE Trans. Geosci. Remote Sens.*, vol. 59, no. 2, pp. 1784–1793, Feb. 2021, doi: 10.1109/TGRS.2020.2998044.

[45] S. Fomel, "Applications of plane-wave destruction filters," *Geophysics*, vol. 67, no. 6, pp. 1946–1960, 2002.

[46] S. Fomel, "Predictive painting of 3D seismic volumes," *Geophysics*, vol. 75, no. 4, pp. A25–A30, Jul. 2010.

[47] A. T. de Hoop, A. Abubakar, and T. M. Habashy, "The contrast-source stress-velocity integral-equation formulation of three-dimensional time-domain elastodynamic scattering problems: A structured approach using tensor partitioning," *J. Acoust. Soc. Amer.*, vol. 126, no. 4, p. 1095, 2009.

[48] G. S. Martin, R. Wiley, and K. J. Marfurt, "Marmousi2: An elastic upgrade for Marmousi," *Lead. Edge*, vol. 25, no. 2, pp. 156–166, Jan. 2006.

[49] Q. Guo, H. Zhang, F. Han, and Z. Shang, "Prestack seismic inversion based on anisotropic Markov random field," *IEEE Trans. Geosci. Remote Sens.*, vol. 56, no. 2, pp. 1069–1079, Feb. 2018.

[50] J. Claerbout. (1999). *Geophysical Estimation By Example: Stanford Exploration Project*. [Online]. Available: http://sepwww.stanford.edu/sep/prof/

[51] J. Claerbout, "Multidimensional recursive filters via a helix," *Geophysics*, vol. 63, no. 5, pp. 1532–1541, 1998.

Cong Luo received the B.S. and M.S. degrees in exploration geophysics from China University of Petroleum, Qingdao, China, in 2012 and 2015, respectively, and the Ph.D. degree in exploration geophysics from China University of Petroleum (Beijing), Beijing, China, in 2019.

She is currently a Post-Doctoral Researcher with Hohai University, Nanjing, China. Her research interests include seismic inversion for isotropic and anisotropic media.

Jing Ba received the B.S. degree in geophysics from Yunnan University, Kunming, China, in 2001, the M.S. degree in geophysics from the Institute of Geology, China Earthquake Administration, Beijing, China, in 2004, and the Ph.D. degree in mechanics from Tsinghua University, Beijing, in 2008.

He is currently a Professor with Hohai University, Nanjing, China. His research interests include rock physics theory, seismic forwarding modeling, and reservoir identification.

Guangtan Huang received the B.S. and M.S. degrees in exploration geophysics from China University of Petroleum, Qingdao, China, in 2012 and 2015, respectively, and the Ph.D. degree in exploration geophysics from China University of Petroleum (Beijing), Beijing, China, in 2019.

He is currently an Assistant Researcher with the Institute of Rock and Soil Mechanics, Chinese Academy of Sciences, Wuhan, China. His research interests include seismic forward modeling and high-resolution seismic inversion.

José M. Carcione received the "Licenciado in Ciencias Físicas" degree from the University of Buenos Aires, Buenos Aires, Argentina, in 1978, the "Dottore in Fisica" degree from the University of Milan, Milan, Italy, in 1984, and the Ph.D. degree in geophysics from Tel-Aviv University, Tel Aviv, Israel, in 1987.

He is currently a Senior Geophysicist at the National Institute of Oceanography and Applied Geophysics (OGS), Trieste, Italy. His research interests include numerical modeling, the theory of wave propagation in acoustic and electromagnetic media, and their application to geophysics.